Effects of the compression rates on the lattice parameters in Zn investigated by dynamic diamond anvil cell

C. Plueckthun,[1,*] J. M. Kaa,[2,†] N. Giordano,[1] R. Husband,[1] M. Schoelmerich,[3,‡] S. Merkel,[4] R. Redmer,[5] and Z. Konopkova[6]

[1]*Deutsches Elektronen-Synchrotron DESY, 22603 Hamburg, Germany*

[2]*TU Dortmund, 44227 Dortmund, Germany*

[3]*Paul Scherrer Institut, Forschungsstrasse 111, 5232 Villigen, Switzerland*

[4]*Univ. Lille, CNRS, INRAE, Centrale Lille, UMR 8207-UMET-Unité Matériaux et Transformations, F-59000 Lille, France*

[5]*Universität Rostock, Institut für Physik, 18051 Rostock, Germany*

[6]*European XFEL, Holzkoppel 4, 22869 Schenefeld, Germany*

(Received 16 May 2025; revised 16 July 2025; accepted 29 July 2025; published 2 September 2025)

High-pressure experiments allow us to induce and control chemical reactions or synthesize materials of unique properties. Furthermore, they are our primary means to replicate the conditions of geological processes and thus of studying, measuring, and understanding compositions and conditions in planetary interiors or asteroid impacts and subduction, etc. In all those experiments, time is a critical factor, as the compression rate or strain rate defines and alters the sample environment. Until recently, most experiments have been performed with either quasistatic strain rates, $\leqslant 10^{-3}\,\mathrm{s}^{-1}$, in diamond anvil cell and large volume press apparatus, or at very high strain rates, $\geqslant 10^{5}\,\mathrm{s}^{-1}$, using gas gun, laser shock, and ramp compression. The work presented here focuses on intermediate compression rates applied to hcp Zn, using the dynamic diamond anvil cell. The evolution of the lattice parameters depends on the choice of the pressure transmitting medium. Nevertheless, at nonhydrostatic conditions we observe a significant change in the evolution of the lattice parameter when compressed at strain rates of $2\times10^{-2}\,\mathrm{s}^{-1}$ or $2.7\times10^{2}\,\mathrm{s}^{-1}$. At $2.7\times10^{2}\,\mathrm{s}^{-1}$, the c/a ratio does not correlate with the results of slow nonhydrostatic experiments, but its trend resembles closer with hydrostatic, quasistatic data. The deviation indicates that strain rates of $2.7\times10^{2}\,\mathrm{s}^{-1}$ interfere with the otherwise predominant deformation mechanism at quasistatic conditions.

DOI: 10.1103/m616-lzw7

I. INTRODUCTION

The c/a ratio for an ideal hcp structure is $\sqrt{8/3} = 1.633$ [1]. Zinc (Zn) is a hexagonal close-packed (hcp) metal with an unusually large c/a ratio of 1.856 at ambient conditions, comparable only to 1.886 of cadmium [1]. The distinctive large c/a ratio has long been a topic of debate. Despite findings suggesting factors such as the potential dominance of specific bonding contributions [2], e.g., bonding through hybridization of the d bands [3–6] or alterations in the Fermi surface [1,7], our understanding of Zn's crystal structure, particularly its axial ratio, remains incomplete and has prompted investigations into the behavior of Zn under compression.

Under compression, the c/a ratio has been reported to decrease, down to a value of $\sqrt{3}$ ($\approx$1.73), approximately 10 GPa. Beyond this critical threshold of c/a, further compression leads to diverging trends, which appear to depend on the degree of hydrostaticity [8]. A hydrostatic pressure transmitting medium, helium (He), resulted in a continuous linear decrease, whereas nonhydrostatic stress conditions, such as those induced by a methanol-ethanol-water (MEW) mixture, lead to a sudden drop in the c/a ratio beyond c/a: $\sqrt{3}$ [8–10]. The discrepancies may arise from varying strain and stress conditions during experiments, influenced by the choice of the pressure transmitting medium (PTM) or experimental method [11]. Prior findings by total-energy-electronic-structure calculations [12] and an experimental DAC study [11] observed a change of the c/a ratio development between 8 to 10 GPa, at $V/V_0 = 0.91-0.89$. The studies by Takemura were triggered by these and earlier investigations by Lynch and Drickamer (1965), suggesting a significant increase in the c/a ratios at $V/V_0 = 0.95$ [1], a finding later corroborated by Sharma *et al.* (1992) [13] at $V/V_0 = 0.94$.

In recent years, interest has shifted toward identifying the primary deformation mechanisms in hcp metals, driven by their industrial applications [14–20] and the significance of hcp phases in planetary sciences [21–24]. In this work, the evolution of the c and a axes is used as a parameter to

*Contact author: christian.plueckthun@desy.de; Also at European XFEL GmbH, 22869 Schenefeld, Germany and Universität Rostock, Institut für Physik, 18051 Rostock, Germany.

†Also at European XFEL GmbH, 22869 Schenefeld, Germany.

‡Also at European XFEL GmbH, 22869 Schenefeld, Germany and Universität Rostock, Institut für Physik, 18051 Rostock, Germany.

identify and discuss changes in the deformation mechanisms of Zn, while it is compressed in a dynamic diamond anvil cell (dDAC) under hydrostatic and nonhydrostatic conditions. With higher load rates, one has to find a balance of a reasonable time resolution and data quality needed for the analysis. Zn is subject to compression rates ranging from 2.9 GPa/s to 32.5 TPa/s, corresponding to intermediate strain rates of the order of 10^{-2} to 10^{2} s^{-1}. The compression rate refers to the maximum pressure change per second, while the volumetric strain rate, hereafter strain rate, applies to the sample, describing the unit cell volume change ($\Delta V/V_0$) over time (s^{-1}). By comparing the results under hydrostatic and nonhydrostatic conditions, we demonstrate that the compression rate significantly influences the evolution of the c/a ratio.

II. MATERIALS AND METHODS

Compression experiments were conducted using the dDAC platform described by Jenei *et al.* [25–27] at the Extreme Conditions beamline, P02.2, PETRA III, DESY [28]. Zn powder (99.995% purity, Sigma-Aldrich/Merck: 324 930) was loaded into 200-μm-thick rhenium (Re) gaskets, which were preindented to 30 μm. The gaskets were placed between 300 μm culet diamonds of symmetric DACs, enabling pressures of 18–38 GPa at a piezoelectric actuator voltage of 400–600 V, which ensured reusability of the diamond anvils after each cycle. Ramp profiles and resulting pressures are shown in Fig. 1. A total of four dDAC (hereafter $L1_{Ne}$, L2, $L3_{Ne}$, and L4) were prepared, resulting in a total of eight—four initial, and four consecutive—room temperature compression and decompression cycles. $L1_{Ne}$ and $L3_{Ne}$ were loaded with neon (Ne), providing hydrostatic conditions, using the gas loading system at the Extreme Conditions Science Infrastructure (ECSI), PETRA III, DESY, Hamburg, Germany. L2 and L4 were loaded without a PTM, inducing nonhydrostatic conditions, Table S.I. Angle-dispersive x-ray powder diffraction (XRD) images were collected using two LAMBDA GaAs 2M detectors [29], D_1 and D_2. The photon energy was set to 25.6 keV and the x-ray beam was focused down to 8 (horizontal) x 3 (vertical) μm^2 FWHM using compound reflective lenses [28]. A Cr_2O_3 standard (NIST SRM 647b) was used to calibrate the detector distance, tilt and rotation and to correct for instrumental broadening. The open source software package DIOPTAS [30] was used for data analysis and azimuthal integration of the raw XRD data. The integrated data were processed using a Python peak fitting routine based on the pseudo-Voigt function along with baseline corrections, which resulted in the determination of the lattice parameters, unit cell volume, and microstrain. The detectors were off-centered in respect to the incident beam position, providing angular, 2Θ, coverages of (D_2) $10-26^\circ$ and (D_1) $15-30^\circ$ for the two detectors, respectively. This configuration enabled the detection of lattice planes (002, 100, 101, 102, $2\bar{1}0$, 103, 004, $2\bar{1}2$, 200, 201) on D_2 and (102, $2\bar{1}0$, 103, 004, $2\bar{1}2$, 200, 201, 104, 202) on D_1, see Supplemental Material Figs. S.1 and 2 [31]. No standard calibrants, such as Au or Pt, were used in either of the loadings to avoid overlap between their high-intensity Bragg reflections and the low-intensity peaks of the sample and to inhibit these calibrants from influencing the compression mechanism. Pressure was instead determined based on

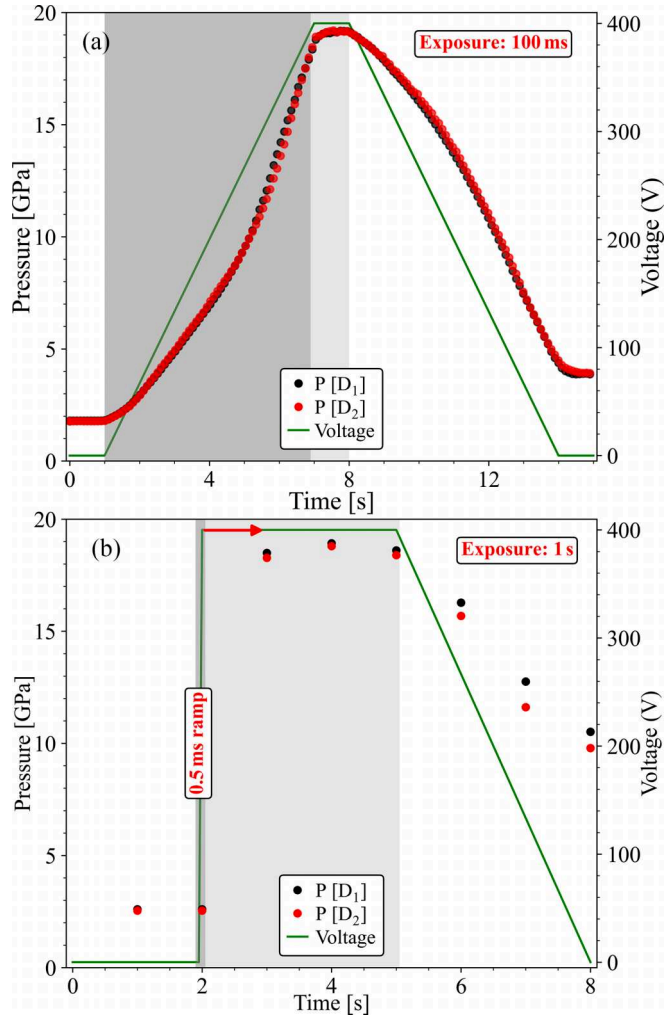

FIG. 1. The voltage applied to the piezoelectric actuator (solid line, right axis) and corresponding pressure response (circles, left axis) are shown as a function of time and as recorded by two LAMBDA detectors (D_1 and D_2). [(a), L2)] A slow, continuous trapezoidal ramp profile, reaching a maximum strain rate of 2×10^{-2} s^{-1} and [(b), L4] a steplike profile achieving a strain rate of 2.7×10^{2} s^{-1}. The shadowed area highlights the interval of (1) an increasing or high compression rate (dark-gray) and (2) decreasing compression rate or constant load (light gray).

$V_0 = 30.450$ (4) [10] and the Zn equation of state (EoS) obtained by Errandonea *et al.* [32], $K_0 = 63$ $K_0' = 5.6$, and Takemura [9,10], $K_0 = 58$ $K_0' = 6$. Despite the absence of a calibrant, only three (D_1) to six (D_2) Bragg diffraction features persisted in all individual exposures.

III. RESULTS

A summary of the conditions for the four initial compression experiments is presented in Table I. Representative batch views of the azimuthal integration as a function of time are given in Supplemental Material Figs. S.4–S.7 [31]. Four consecutive cycles were measured in L2 and $L3_{Ne}$, Table S.I. A one-to-one comparison with the initial cycles is not possible, because the starting conditions, e.g., strain, grain size and lattice preferred orientation (LPO) are altered by

TABLE I. Overview of the experimental conditions of the four loaded cells, using 300 μm culet diamonds with Re gaskets. Loadings with Ne (PTM) and without to investigate hydrostatic and nonhydrostatic condition, respectively.

Loading	Sample (PTM)	P_{start} (GPa)	Exposure (ms)	Number of images	Voltage max. (V)	Type	Comp rate Ø	Strain rate Ø s^{-1}
$L1_{Ne}$	Zn (Ne)	1.0	100	180	400	trapezoidal	3.8 GPa/s	3×10^{-2}
L2	Zn	1.7	100	150	400	trapezoidal	2.9 GPa/s	2×10^{-2}
$L3_{Ne}$	Zn (Ne)	0.9	20	55	400	trapezoidal	40 GPa/s	3×10^{-1}
L4	Zn	2.4	1000	8	400	step	32.5 TPa/s	2.7×10^{2}

preceding cycles. Nevertheless, the results are interesting, providing information about the effect of multiple events and different ramp intervals and can be found in Supplemental Material D [31]. Figure 2 shows the lattice parameter evolution as a function of pressure and V/V_0 during the initial compression events at the different compression rates. In Fig. 2(a), the a and c axes show a linear decrease up to about 10 GPa, $V/V_0 = 0.89$, and the c axis compresses ≈4.5x faster than the a axis. Beyond 10 GPa, $V/V_0 = 0.89$, loadings with compression rates $\leqslant 4$ GPa/s ($L1_{Ne}$ and L2) show a slightly faster decrease in the c axis, while the a axis becomes less compressible.

$L1_{Ne}$ and L2, $3\times10^{-2}\,s^{-1}$ and $2\times10^{-2}\,s^{-1}$, respectively, closely mimic the trend observed within MEW by Takemura [9]. The close correlation of $L1_{Ne}$ with the trend in MEW [9] can be explained by the partial collapse of the gasket hole, causing one side of the sample to come in direct contact with the Re gasket, thus involuntarily yielding a nonhydrostatic environment. L2 represents nonhydrostatic conditions at slow strain rates: $2\times10^{-2}\,s^{-1}$. In Fig. 2(b), at strain rates of $3\times10^{-1}\,s^{-1}$, $L3_{Ne}$, the a axis hardening beyond 10 GPa is inhibited and both axes compress monotonously. The data show a close correlation with the hydrostatic data by Takemura [8]. Interestingly, the data recorded in runs L4 and $L3_{Ne}$ match well with each other.

Figure 3 presents the c/a ratio of Zn as a function of relative volume (V/V_0) during the initial compression cycles of L2, $L3_{Ne}$, and L4. We discuss the data of $L1_{Ne}$ only in Supplemental Material C [31], as the c/a ratio evolution of $L1_{Ne}$ and L2 are very similar. The hydrostatic evolution, He PTM, by Takemura [8] and nonhydrostatic data obtained in L2, collected at slow, intermediate strain rates, $2\times10^{-2}\,s^{-1}$, show a consistent c/a ratio evolution up to 10 GPa, down to a c/a ratio of $\approx\sqrt{3}$. Beyond 10 GPa, the c/a ratio under nonhydrostatic conditions decreases faster and the trend shows close similarity to the MEW PTM data by Takemura [9]. In contrast, the data beyond 16 GPa, collected across the constant load interval of hydrostatic $L3_{Ne}$, with intermediate strain rates of $3\times10^{-1}\,s^{-1}$, match with the hydrostatic He PTM data by Takemura [8]. However, in between the 8 to 16 GPa interval, our data show increased c/a ratios, only partially comparable to previous findings by Errandonea *et al.* [32] at 300 K, whom used a NaCl PTM. L4, exhibiting strain rates of $2.7\times10^{2}\,s^{-1}$, deviates significantly from its slow, nonhydrostatic counterpart, L2, $2\times10^{-2}\,s^{-1}$. It is evident that L2 records c/a ratios that are lower than previous findings in MEW PTM [8], whereas L4 depicts c/a ratios, trending toward observations under hydrostatic conditions.

The microstrain evolution, Fig. 4, was obtained following the procedure by Singh *et al.* [33,34], using the FWHM of the Bragg reflections as a measure to quantify the strain within the sample. The microstrain analysis across the compression intervals is affected by peak broadening because of the peak shift resulting from the pressure change in a XRD image acquisition. In L2, Fig. 4(a), the development of the microstrain is delayed compared to the pressure dependence, proving nonhydrostatic conditions at $2\times10^{-2}\,s^{-1}$. In contrast, $L3_{Ne}$, Fig. 4(b), at $3\times10^{-1}\,s^{-1}$, demonstrates accumulation of microstrain almost exclusively during the first half of the compression interval and a release thereafter. An evolution that proves sustainment of hydrostatic conditions throughout the entire event. The high-resolution record in each XRD image of L2, small pressure increments of 0.1 to 0.6 GPa, should result in an insignificant or small effect on the general microstrain trend, yet may slightly alter the maximum. However, most likely its effect accounts for the majority of the variations recorded during compression of $L3_{Ne}$ because of larger pressure intervals of 0.2 to 2.5 GPa and also during the decompression of L4. Consistent with previous reports, e.g., Konopkova *et al.* [35], the nonhydrostatic loadings accumulate higher microstrain during the event compared to those with a PTM. We record the highest persisting microstrain: $\eta = 1.2\times10^{2}$ at fast, intermediate strain rates, $2.7\times10^{2}\,s^{-1}$, L4, Fig. 4(c). However, at constant high load the c/a ratios in L4 differ significantly from those in L2, $2\times10^{-2}\,s^{-1}$. In L4, we do not have the data for changes during compression and choose longer acquisitions at constant load to investigate a possible delay in the microstrain and pressure dependence. In contrast to L2, where the microstrain accumulation persists even into the decompression interval, no extended delay is observed across the constant load interval of L4. Further changes are only observed during decompression, where peak broadening is induced as pressure changes during the acquisition. In contrast to L2, the microstrain in L4 shows only a slight decrease with the release of the load from the piezoelectric actuator compared to the conditions at constant high load.

IV. DISCUSSION

A. The c/a ratio: $\sqrt{3}$

We presented the meticulously resolved lattice parameter evolution of Zn at nonhydrostatic conditions during a single compression event, L2, at slow, intermediate strain rates $2\times10^{-2}\,s^{-1}$ and up to approximately 19.2 GPa. Takemura [9] initially observed a singularity at $c/a = \sqrt{3}$, which he later revoked, using He as a PTM [8]. In 1995, the apparent

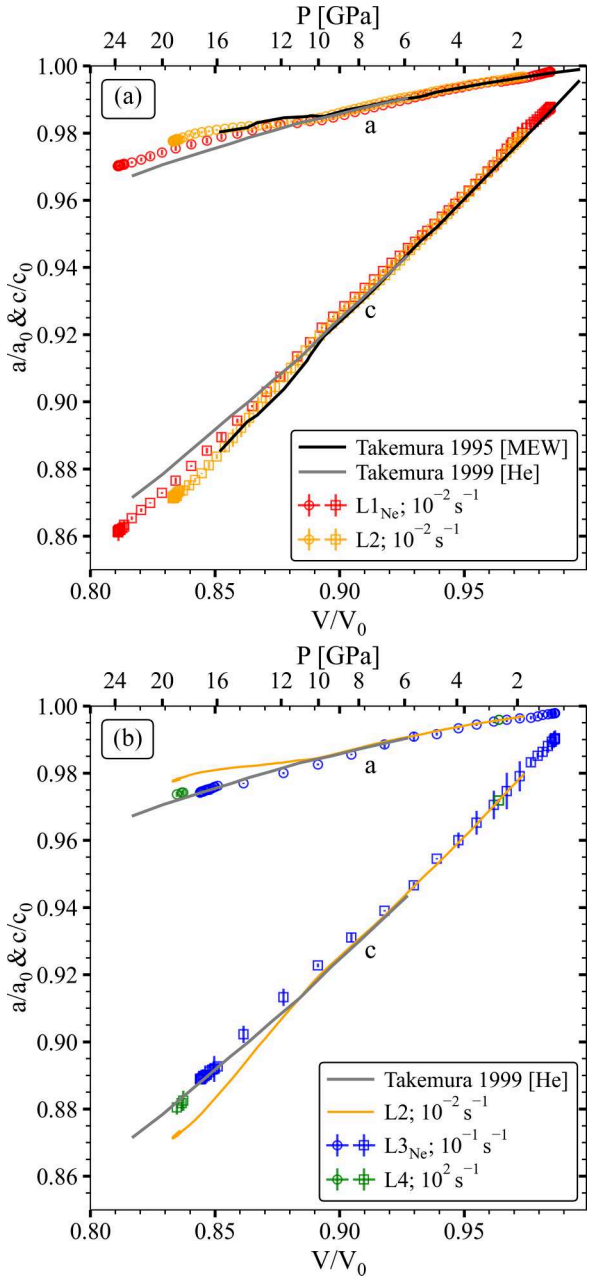

FIG. 2. Zinc (Zn) lattice parameter ratio a/a_0 and c/c_0 as a function of volume during the first cycle. (a) The results of $L1_{Ne}$ and L2 are depicted as red and orange open circles and squares. The results of Takemura [8,9], in MEW, PTM, and He are plotted as black and gray solid lines. (b) The results of the $L3_{Ne}$ and L4 are depicted as blue and green open circles and squares. The orange and gray solid lines plot the nonhydrostatic data of L2 and hydrostatic data by Takemura [8].

singularity turned out to be a relic of the solidification and rapid hardening of the PTM (MEW) and resulted in deviatoric stresses at the c/a ratio: $\sqrt{3}$ and the development of strain and LPO. With the robust and highly resolved pressure dependence at nonhydrostatic conditions here reported, we confirm hardening of the a axis and increased collapse of the c axis beyond 10 GPa and c/a ratio: $\sqrt{3}$. The effects of a-axis hardening and c-axis collapse are stronger compared to previous

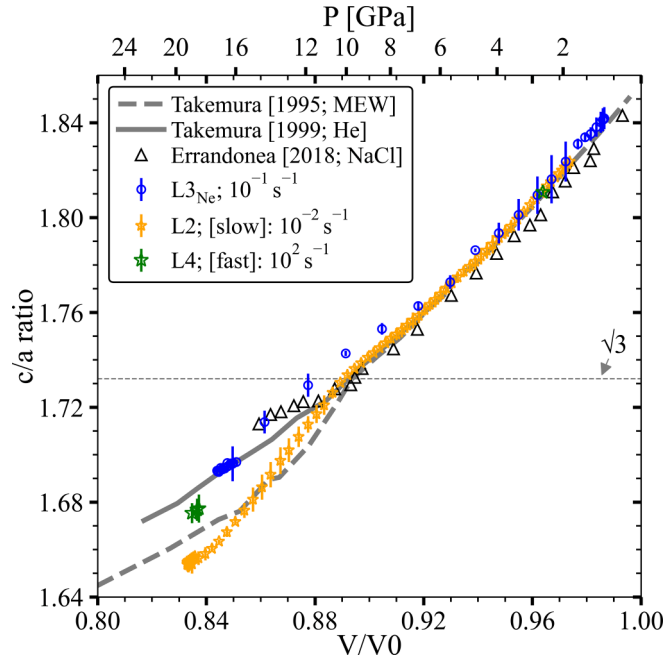

FIG. 3. The c/a ratio of Zn across the compression and constant load interval. The colorful circles and stars represent the results of the initial loadings. Previous data by Takemura [8,9] are shown as a solid (hydrostatic) and dashed (MEW PTM) gray line, while more recent results in the DAC are plotted as black open triangles [32].

data, where the PTM, MEW, or ME (methanol-ethanol) [9] failed to preserve hydrostatic conditions, achieving lower c/a values at 19 GPa. Despite the lower c/a values at 19 GPa, we observe a gentler initial decline beyond the c/a ratio: $\sqrt{3}$ and up to 16 GPa, Fig. 3. This trend is most likely a remnant of our measurement methodology, as our data consists of a series of consecutive measurements during noninterrupted ramps and do not represent quasistatic conditions after a finite pressure increase, with the sole exception of L4. The critical factor in our experiments is the varying time the sample has to adapt to its environment. Its influence is obvious in $L3_{Ne}$. $L3_{Ne}$, 3×10^{-1} s^{-1}, shows c/a ratios matching He PTM data [8] beyond 16 GPa, meaning at the end of the compression event. However, the data shows higher c/a ratios between 8 to 16 GPa, which is the interval with the highest compression rates during the initialized ramp profile.

B. Methodology

The difference in Zn lattice constant evolution, due to the utilized PTM, has been shown by Takemura [8–10]. Nevertheless, we used Ne instead of He due to the gas loading capabilities available to us at the time of the experiment. Studies by Klotz *et al.* [36] showed that changes in stress distribution, i.e., changes of the linewidth, should be induced only beyond the c/a ratio: $\sqrt{3}$, beyond 15 GPa for Ne and 20 GPa for He. However, as mentioned in the previous section, the comparison of the hydrostatic results, $L3_{Ne}$ and Takemura [8], He PTM shows higher c/a ratios in the interval between 8 to 16 GPa and matches during the constant load interval beyond 16 GPa, Fig. 3. While a higher c/a ratio is most evident over the compression interval in $L3_{Ne}$, similar results

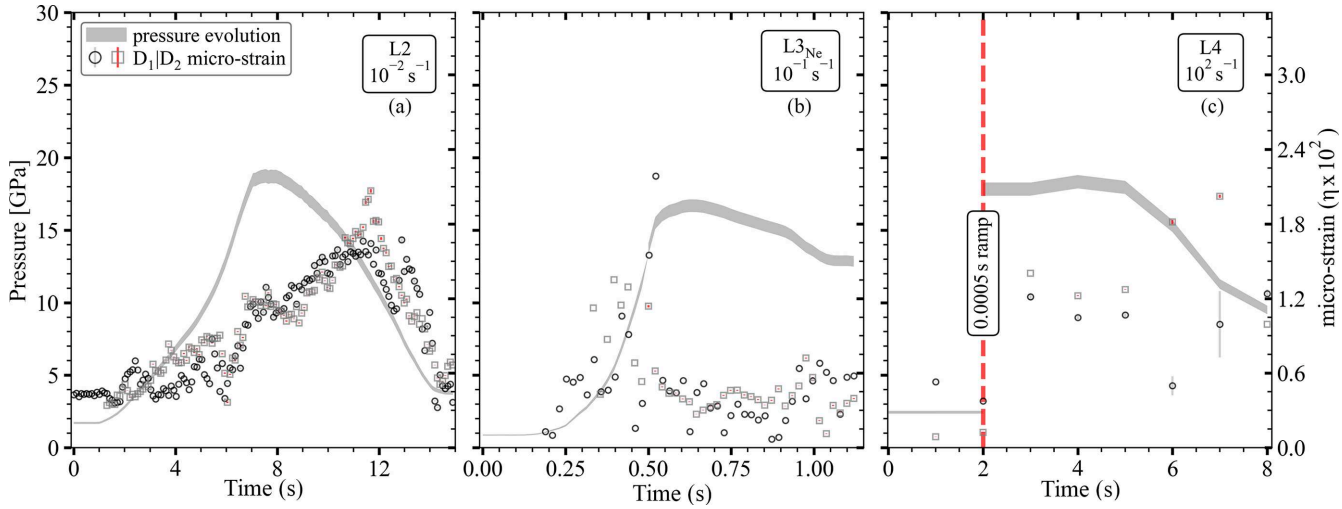

FIG. 4. Microstrain (detectors 1 and 2: D_1 and D_2, respectively) and pressure evolution during the initial cycle of L2 to L4. The pressure range is based on the variance of the EoS [9,32].

are observed during $L1_{Ne}$, 6 to 12 GPa, Fig. 3, and even during L2 which contained no PTM, 12 to 16 GPa. The consistent manifestation of this observation precludes the PTM as the cause of those altered c/a ratios, especially since the difference between hydrostatic and nonhydrostatic conditions observed by Takemura persists clearly in our data. Instead, we believe that the alteration is caused by our measurement methodology. The data consists of a series of consecutive measurements during noninterrupted ramps and were not collected after a finite pressure increase. Our assumption finds support in $L3_{Ne}$, 3×10^{-1} s^{-1}, where the c/a ratio difference is more evident compared to the slow $L1_{Ne}$ and L2, 3×10^{-2} s^{-1} or 2×10^{-2} s^{-1}. Recent experiments by Errandonea *et al.* [32] also showed increasing c/a ratios beyond 12 GPa. The increase may relate to a noninterrupted event because the data was collected with a membrane DAC, yet it may also relate to an altered stress distribution within the utilized solid PTMs, NaCl or MgO. Both PTMs are soft materials commonly used in high-temperature experiments, whereby the rising temperature counteracts the increasing microstrain. However, at ambient temperature, the equalizing relief of microstrain is inhibited. Consequently, changes in grain size, hence grain boundaries of the solid PTM, can alter the sample environment and the accumulation and distribution of microstrain between soft PTM and the sample material. Thus, a direct explanation of their cause of variation is not possible without the methodology.

C. Deformation of zinc

L4 achieved strain rates of 2.7×10^{2} s^{-1} across a nonhydrostatic 0.5 ms ramp. The recorded c/a ratio does not match the data during slow nonhydrostatic compression in L2, 2×10^{-2} s^{-1}. Despite the absence of a PTM, we observe c/a ratios, which are more in line with experiments that tried to provide hydrostatic conditions [9,11]. Yet the data shows even higher c/a ratios, further trending to match slow, hydrostatic measurements [8,32], Fig. 3. However, the microstrain evolution of those two loadings does not support such a similarity, Fig. 4. In hcp metals, different deformation mechanisms are required to deform a polycrystalline sample, depending on the ductility and c/a ratio of the selected phase [37]. These mechanisms have been determined by radial diffraction, deformation DIA experiments and are supported by viscoplastic self-consistent polycrystal plasticity modeling or molecular simulation/molecular dynamic first-principles density functional theory (DFT-MS/MD) [38–44].

In Zn $\{10\bar{1}2\}$, twinning is a key element contributing to the development of texture (LPO) [38,45], and under truly hydrostatic strain it does not favor any specific directions or is mostly inactive. At low pressure and strain, <10 GPa or above the $c/a > \sqrt{3}$, $\{10\bar{1}2\}$ twinning results in c-axis alignment orthogonal to the compression direction while basal slip $\{0002\}\langle2\bar{1}\bar{1}0\rangle$ is the main deformation mechanism [38]. Beyond 10 GPa, $c/a < \sqrt{3}$, the property of $\{10\bar{1}2\}$ twinning changes from compressive to tensile and the c axis flips to be parallel to the compression direction. Nevertheless, basal slip prevails as the main deformation mechanism, whereas tensile twinning is not as prevalent as compressive twinning above $c/a = \sqrt{3}$ [38,45]. Close to or at $c/a \approx \sqrt{3}$, twinning is not observable due to the change of compression to tensile activation [45]. A change of the activity of those two mechanisms, basal slip and twinning, would explain higher c/a ratio, as elongation and compression of the axes are inhibited by time. In hcp metals, twinning was shown to account for fast changes (μs) at ambient temperature, whereas stress relaxation via edge or slip dislocation requires longer timescales (ms) [46]. Furthermore, the effect of the strain rate on the deformation mechanisms was explored for multiple hcp phases, e.g., Refs. [47–49], including beryllium (Be) [39,50]. Be has a higher shear resistivity compared to Zn, but both hcp phases are brittle at ambient temperature, show the same $\{10\bar{1}2\}$ single twinning direction restriction, and are prone to exhibit crack nucleation [37]. Sisneros *et al.* [39] performed deformation at compression rates below 10^{0} s^{-1} and above 10^{3} s^{-1}. They found that both basal slip and twinning act to align the basal poles with the straining direction. At higher strain rates, the twinning activity increases, resulting

in a much faster texture evolution and beyond strain rates of $5\times10^3\,s^{-1}$, twinning is the most active mechanism, as indeed basal slip seems to be inhibited by time. We observe LPO in Figs. S. 9.1 and 9.2 [31], however, due to the nature of the fast compression events, preventing us to rotate the cell during the exposure, determination of the deformation mechanism within the sample is not possible.

Furthermore, an important factor for the variance between $L3_{Ne}$ and L4 could also be the exposure time. In $L3_{Ne}$, hydrostatic, an image was collected across 20 ms, allowing us to meticulously track the development during compression, constant load, and decompression, whereas in L4, nonhydrostatic, all high-pressure data were collected after the compression event and with 1 s exposures. The applied strain rate, $2.7\times10^2\,s^{-1}$, may have been insufficient to fully inhibit stress relaxation and distribution via basal slip during and after the compression event. Both processes may have lowered the c/a ratios.

Another important property of a material is dislocation density. With higher strain rates, dislocations within the material increase, yet recent results by Hansen *et al.* [51] showed that much higher strain rates, $10^8\,s^{-1}$, would be required to affect the axial stress distribution behavior. It should be noted that Ref. [51] aimed to model the deformation of single crystals, hence direct correlation to multigrain or powder samples is not possible and would require additional studies.

V. CONCLUSION

Hydrostatic and nonhydrostatic XRD data of Zn were collected using the dDAC at strain rates spanning five orders of magnitudes ($10^{-2}-10^2\,s^{-1}$), and equivalent to compression rates of $\approx 2.9\,GPa/s - 32.5\,TPa/s$. As described by Takemura [8–10], the c/a ratio depends strongly on the PTM, resulting in divergent trends beyond the c/a ratio: $\sqrt{3}$. Nevertheless, it also depends on competing deformation mechanisms during slow or fast compression. Previous results for beryllium [39] reported that twinning is the preferred deformation mechanism in hcp metals at strain rates of $10^3\,s^{-1}$, with the first observation of its influence appearing at strain rates of $10^0\,s^{-1}$. At lower strain rates ($\leqslant 10^{-1}s^{-1}$), basal slip is the main deformation mechanism [38]. No data were available for strain rates within the range of $10^0-10^3\,s^{-1}$. We observe that at nonhydrostatic conditions L4, intermediate strain rates of the order of $2.7\times10^2\,s^{-1}$ inhibit a-axis hardening and a fast c-axis collapse beyond the c/a ratio: $\sqrt{3}$. The c/a ratio deviates from quasistatic nonhydrostatic conditions and trends to approach quasistatic hydrostatic data. Based on the timescales of different deformation mechanisms [46] and on the deformation mechanisms associated and found in hcp phases [38–44], we propose that the change in c/a ratio is due to an increasing activity of twinning at the intermediate strain rates. To be more specific, the rapid development of twins impedes crystal reorientation. Our findings demand further studies, using different PTMs and a variety of compression rates. Yet, more importantly, it is indispensable to incorporate radial diffraction capabilities [52] to offer the means to investigate *in situ* the LPO and grain size evolution across the fast compression intervals.

ACKNOWLEDGMENTS

This research was supported through the German Science Foundation (DFG) under Grant No. KO-5262/1. S.M. was funded by the European Union (ERC, HotCores, Grant No. 101054994). We acknowledge DESY (Hamburg, Germany), a member of the Helmholtz Association HGF, for the provision of experimental facility PETRA III and especially the crew of ECB P02.2 for their support during the preparation, setup, gas loading, and experiment. We acknowledge B. Winkler and BMBF Project No. 05K13RF1 for purchase of the LAMBDA GaAs 2M detectors and the laser cutting machine for gasket preparation. C.P. thanks H.-P. Liermann and S. Francoual for their support and discussions.

C.P. provided studying material, conceptualized the activities and methodology, supported investigation and validation, performed the data analysis, visualization, and writing. Z.K. acquired funding, supervised and administered the work, helped with methodology, software and provided critical review and commentary. R.R. supervised the work and provided critical review and commentary. S.M. provided critical review and commentary. J.M.K. and M.S. supported investigations and M.S. provided critical review and commentary. R.H. and N.G. supported the experiment at P02.2. R.H. further helped to conceptualize the work and N.G. also provided critical review and commentary.

DATA AVAILABILITY

The data that support the findings of this article are openly available [53]. Access to all raw data is available upon reasonable request to the author.

[1] R. W. Lynch and H. G. Drickamer, The effect of pressure on the resistance and lattice parameters of cadmium and zinc, J. Phys. Chem. Solids **26**, 63 (1965).

[2] D. Weaire, The structures of the divalent simple metals, J. Phys. C **1**, 210 (1968).

[3] W. A. Harrison, Electronic structure and the properties of metals. II. Application to zinc, Phys. Rev. **129**, 2512 (1963).

[4] J. A. Moriarty, Zero-order pseudoatoms and the generalized pseudopotential theory, Phys. Rev. B **10**, 3075 (1974).

[5] J. A. Moriarty, Density-functional formulation of the generalized pseudopotential theory, Phys. Rev. B **16**, 2537 (1977).

[6] J. A. Moriarty, Generalized pseudopotential theory of d-band metals, Int. J. Quantum Chem. **24**, 541 (1983).

[7] W. Potzel, M. Steiner, H. Karzel, W. Schiessl, M. Köfferlein, G. M. Kalvius, and P. Blaha, Electronically driven soft modes in zinc metal, Phys. Rev. Lett. **74**, 1139 (1995).

[8] K. Takemura, Absence of the c/a anomaly in Zn under high pressure with a helium-pressure medium, Phys. Rev. B **60**, 6171 (1999).

[9] K. Takemura, Zn under pressure: A singularity in the hcp structure at $c/a = \sqrt{3}$, Phys. Rev. Lett. **75**, 1807 (1995).

[10] K. Takemura, The zinc story under high pressure, J. Miner. Mater. Charact. Eng. **07**, 354 (2019).

[11] O. Schulte, A. Nikolaenko, and W. B. Holzapfel, Pressure-volume relations for Zn, Cd, Ga, In and TI at room temperature to 30 GPa and above, Intl. J. High Press. Res. **6**, 169 (1991).

[12] S. Meenakshi, V. Vijayakumar, B. K. Godwal, and S. K. Sikka, Distorted hcp structure of zinc under pressure, Phys. Rev. B **46**, 14359 (1992).

[13] S. M. Sharma, S. K. Sikka, and R. Chidambaram, *Recent Trends in High Pressure Research*, edited by A. K. Singh (Oxford & IBH Publishing Co., New Delhi, 1992), p. 878.

[14] R. Parisot, S. Forest, A. Pineau, F. Grillon, X. Demonet, and J.-M. Mataigne, Deformation and damage mechanisms of zinc coatings on hot-dip galvanized steel sheets: Part I. Deformation modes, Metall. Mater. Trans. A **35**, 797 (2004).

[15] C. Cui, B. Hu, L. Zhao, and S. Liu, Titanium alloy production technology, market prospects and industry development, Mater. Des. **32**, 1684 (2011).

[16] Y. Song, E.-H. Han, D. Shan, C. D. Yim, and B. S. You, The effect of Zn concentration on the corrosion behavior of Mg-*x*Zn alloys, Corros. Sci. **65**, 322 (2012).

[17] A. A. Luo, Magnesium casting technology for structural applications, J. Magnesium and Alloys **1**, 2 (2013).

[18] T. B. Britton, F. P. E. Dunne, and A. J. Wilkinson, On the mechanistic basis of deformation at the microscale in hexagonal close-packed metals, Proc. R. Soc. A **471**, 20140881 (2015).

[19] Z. Wu, H. Kou, N. Chen, Z. Xi, J. Fan, B. Tang, and J. Li, Recent developments in cold dwell fatigue of titanium alloys for aero-engine applications: a review, J. Mater. Res. Technol. **20**, 469 (2022).

[20] D. König, T. Vermeij, F. Maresca, and J. P. M. Hoefnagels, Direct comparison of nanoscale plasticity in single and bi-crystal tensile tests extracted from a zinc coating, Mater. Sci. Eng., A **932**, 148128 (2025).

[21] Y. Ma, M. Somayazulu, G. Shen, H.-K. Mao, J. Shu, and R. J. Hemley, *In situ* x-ray diffraction studies of iron to earth-core conditions, Phys. Earth Planet. Inter. **143-144**, 455 (2004).

[22] M. I. Bergman, J. Yu, D. J. Lewis, and G. K. Parker, Grain boundary sliding in high-temperature deformation of directionally solidified hcp Zn alloys and implications for the deformation mechanism of Earth's inner core, J. Geophys. Res.: Solid Earth **123**, 189 (2018).

[23] R. G. Kraus, R. J. Hemley, S. J. Ali, J. L. Belof, L. X. Benedict, J. Bernier, D. Braun, R. E. Cohen, G. W. Collins, F. Coppari, M. P. Desjarlais, D. Fratanduono, S. Hamel, A. Krygier, A. Lazicki, J. Mcnaney, M. Millot, P. C. Myint, M. G. Newman, J. R. Rygg *et al.*, Measuring the melting curve of iron at super-Earth core conditions, Science **375**, 202 (2022).

[24] S. A. Hunt, A. M. Walker, O. T. Lord, S. Stackhouse, L. Schardong, L. S. Armstrong, A. J. Parsons, G. E. Lloyd, J. Wheeler, D. M. Fenech, S. Michalik, and M. L. Whitaker, Experimental observation of a new attenuation mechanism in *hcp*-metals that may operate in the Earth's inner core, Geochem. Geophys. Geosyst. **25**, e2023GC011386 (2024).

[25] Zs. Jenei, H.-P. Liermann, R. Husband, A. S. J. Méndez, D. Pennicard, H. Marquardt, E. F. O'Bannon, A. Pakhomova, Z. Konopkova, K. Glazyrin, M. Wendt, S. Wenz, E. E. McBride, W. Morgenroth, B. Winkler, A. Rothkirch, M. Hanfland, and W. J. Evans, New dynamic diamond anvil cells for tera-pascal per second fast compression x-ray diffraction experiments, Rev. Sci. Instrum. **90**, 065114 (2019).

[26] W. J. Evans, C. S. Yoo, G. W. Lee, H. Cynn, M. J. Lipp, and K. Visbeck, Dynamic diamond anvil cell (dDAC): A novel device for studying the dynamic-pressure properties of materials, Rev. Sci. Instrum. **78**, 073904 (2007).

[27] R. J. Husband, E. F. O'Bannon, H.-P. Liermann, M. J. Lipp, A. S. J. Mendez, Z. Konopkova, E. E. McBride, W. J. Evans, and Z. Jenei, Compression-rate dependence of pressure-induced phase transitions in Bi, Sci. Rep. **11**, 14859 (2021).

[28] H.-P. Liermann, Z. Konôpková, W. Morgenroth, K. Glazyrin, J. Bednarčik, E. E. McBride, S. Petitgirard, J. T. Delitz, M. Wendt, Y. Bican, A. Ehnes, I. Schwark, A. Rothkirch, M. Tischer, J. Heuer, H. Schulte-Schrepping, T. Kracht, and H. Franz, The extreme conditions beamline P02.2 and the extreme conditions science infrastructure at PETRA III, J. Synchrotron Radiat. **22**, 908 (2015).

[29] D. Pennicard, S. Smoljanin, F. Pithan, M. Sarajlic, A. Rothkirch, Y. Yu, H.-P. Liermann, W. Morgenroth, B. Winkler, Z. Jenei, H. Stawitz, J. Becker, and H. Graafsma, LAMBDA 2M GaAs—A multi-megapixel hard x-ray detector for synchrotrons, J. Instrum. **13**, C01026 (2018).

[30] C. Prescher and V.B. Prakapenka, DIOPTAS: A program for reduction of two-dimensional x-ray diffraction data and data exploration, High Press. Res. **35**, 223 (2015).

[31] See Supplemental Material at https://link.aps.org/supplemental/10.1103/m616-lzw7 for the data of the experiment, which includes Refs. [54,55].

[32] D. Errandonea, S. G. MacLeod, J. Ruiz-Fuertes, L. Burakovsky, M. I. McMahon, C. W. Wilson, J. Ibañez, D. Daisenberger, and C. Popescu, High-pressure/high-temperature phase diagram of zinc, J. Phys.: Condens. Matter **30**, 295402 (2018).

[33] A. K. Singh, C. Balasingh, H. K. Mao, R. J. Hemley, and J. Shu, Analysis of lattice strains measured under nonhydrostatic pressure, J. Appl. Phys. **83**, 7567 (1998).

[34] A. K. Singh, A. Jain, H.-P. Liermann, and S. K. Saxena, Strength of iron under pressure up to 55 GPa from x-ray diffraction line-width analysis, J. Phys. Chem. Solids **67**, 2197 (2006).

[35] Z. Konôpková, A. Rothkirch, A. K. Singh, S. Speziale, and H. P. Liermann, *In situ* x-ray diffraction of fast compressed iron: Analysis of strains and stress under non-hydrostatic pressure, Phys. Rev. B **91**, 144101 (2015).

[36] S. Klotz, J.-C. Chervin, P. Munsch, and G. Le Marchand, Hydrostatic limits of 11 pressure transmitting media, J. Phys. D **42**, 075413 (2009).

[37] M. H. Yoo, Slip, twinning, and fracture in hexagonal close-packed metals, Metall. Trans. A **12**, 409 (1981).

[38] W. Kanitpanyacharoen, S. Merkel, L. Miyagi, P. Kaercher, C. N. Tomé, Y. Wang, and H. R. Wenk, Significance of mechanical twinning in hexagonal metals at high pressure, Acta Mater. **60**, 430 (2012).

[39] T. A. Sisneros, D. W. Brown, B. Clausen, D. C. Donati, S. Kabra, W. R. Blumenthal, and S. C. Vogel, Influence of strain rate on mechanical properties and deformation texture of hot-pressed and rolled beryllium, Mater. Sci. Eng. A **527**, 5181 (2010).

[40] S. Merkel, H.-R. Wenk, P. Gillet, H.-K. Mao, and R. J. Hemley, Deformation of polycrystalline iron up to

30 GPa and 1000 K, Phys. Earth Planet. Inter. **145**, 239 (2004).

[41] S. Merkel, C. Tomé, and H.-R. Wenk, Modeling analysis of the influence of plasticity on high pressure deformation of hcp-Co, Phys. Rev. B **79**, 064110 (2009).

[42] L. Miyagi, M. Kunz, J. Knight, J. Nasiatka, M. Voltolini, and H.-R. Wenk, *In situ* phase transformation and deformation of iron at high pressure and temperature, J. Appl. Phys. **104**, 103510 (2008).

[43] G. Liu, J. Wang, and Y. Shen, Density functional theory study of $\{10\bar{1}n\}$ twin boundaries of Zn under high pressure, Comput. Mater. Sci. **151**, 106 (2018).

[44] H.-R. Wenk, S. Matthias, R. J. Hemley, H.-K Mao, and J. Shu, The plastic deformation of iron at pressures of the Earth's inner core, Nature (London) **405**, 1044 (2000).

[45] S. Merkel, N. Hilairet, Y. Wang, J. Guignard, and C. N. Tomé, Androgynous $\{10\bar{1}2\}$ twin in zinc, Phys. Rev. Mater. **8**, 063603 (2024).

[46] N. V. Kamyshanchenko, I. S. Nikulin, E. S. Kungurtsev, and M. S. Kungurtsev, Experimental determination of preferential mechanisms of stress relaxation during deformation of HCP metals, Tech. Phys. Lett. **39**, 469 (2013).

[47] S. G. Song and G. T. Gray, Influence of temperature and strain rate on slip and twinning behavior of Zr, Metall. Mater. Trans. A **26**, 2665 (1995).

[48] G. T. Gray, Influence of strain rate and temperature on the structure. Property behavior of high-purity titanium, J. Phys. IV France **07**, C3 (1997).

[49] E. Cerreta and G. T. Gray III, The influence of texture, strain rate, temperature, and chemistry on the mechanical behavior of hafnium, Metall. Mater. Trans. A **35**, 1999 (2004).

[50] D. W. Brown, S. P. Abeln, W. R. Blumenthal, M. A. M. Bourke, M. C. Mataya, and C. N. Tomé, Development of crystallographic texture during high rate deformation of rolled and hot-pressed beryllium, Metall. Mater. Trans. A **36**, 929 (2005).

[51] B. L. Hansen, I. J. Beyerlein, C. A. Bronkhorst, E. K. Cerreta, and D. Dennis-Koller, A dislocation-based multi-rate single crystal plasticity model, Int. J. Plast. **44**, 129 (2013).

[52] L. Q. Huston, L. Miyagi, R. J. Husband, K. Glazyrin, C. Kiessner, M. Wendt, H. P. Liermann, and B. T. Sturtevant, New dynamic diamond anvil cell for time-resolved radial x-ray diffraction, Rev. Sci. Instrum. **95**, 043904 (2024).

[53] C. Plückthun, J. M. Kaa, N. Giordano, R. Husband, M. Schoelmerich, S. Merkel, R. Redmer, and Z. Konopkova, Zinc (Zn) DAC ramp dataset storage (dynamic, membrane etc.). (1.0.0) [Data set], Zenodo, (2025), https://doi.org/10.5281/zenodo.15364085

[54] D. B. McWhan, Compressibility of cadmium and zinc to 100 kbar, J. Appl. Phys. **36**, 664 (1965).

[55] D. B. McWhan and W. L. Bond, Simple high pressure x-ray powder camera, Rev. Sci. Instrum. **35**, 626 (1964).